Hindawi
International Transactions on Electrical Energy Systems
Volume 2023, Article ID 1152243, 19 pages
https://doi.org/10.1155/2023/1152243

Research Article

Design and Simulation Analysis of Stator Slots for Small Power Permanent Magnet Brushless DC Motors

Chuanhui Zhu, Rujie Lu, Congli Mei, Tao Peng, and Guoqin Zhang

Zhejiang University of Water Resources and Electric Power, Hangzhou 310018, China

Correspondence should be addressed to Chuanhui Zhu; zhchh@zjweu.edu.cn

Received 7 December 2022; Revised 31 December 2022; Accepted 2 February 2023; Published 16 February 2023

Academic Editor: Flah Aymen

Copyright © 2023 Chuanhui Zhu et al. This is an open access article distributed under the Creative Commons Attribution License, which permits unrestricted use, distribution, and reproduction in any medium, provided the original work is properly cited.

With the development of power electronics technology, permanent magnet brushless DC motors have developed rapidly and are now widely used in electric vehicles, flywheel energy storage, rail transit, and other applications. The stator slot structure is one of the main factors affecting the performance of the motor. A low-power permanent magnet brushless DC motor was selected as the research object, and the finite element analysis method was used to study the effects of different slot and pole combinations and stator slot types on the cogging torque, reluctance torque, and back electromotive force of the permanent magnet brushless DC motor. The influence of the stator slot structure of the motor on the performance of the motor was analyzed, and the optimal slot-pole combination and stator slot type were determined. The results showed that the cogging torque of the 2-stage 24-slot motor was 14 mN·m, and the reluctance torque was 75 mN·m. The cogging torque and reluctance torque were the smallest, and the back electromotive force waveform was similar to a trapezoidal wave. The motor cogging torque of the pear-shaped round slot was the smallest, with a value of 460 mN·m, and the motor reluctance torque of the pear-shaped trapezoidal slot was the smallest, with a value of 1.2 N·m. The back electromotive force waveforms of the motors with four different stator slot types were similar.

1. Introduction

In 1962, T.G. Wilson of Duke University and P.H. Trickey of Wright Machinery Company filed a patent titled "solid-state commutation DC motor," and subsequently, the first brushless direct current (DC) motors in the world were developed. With a brushless DC motor, the mechanical commutator in the traditional DC motor is replaced by an electronic commutator [1]. The permanent magnet brushless DC motor is a brushless DC motor that generates a main magnetic field through a permanent magnet. There are many classifications of permanent magnet brushless DC motors. For example, the design of a permanent magnet brushless DC motor using a fractional slot can improve the efficiency and power density, improve the motor rotation speed, and make the motor a high-speed permanent magnet brushless DC motor. Compared with an ordinary permanent magnet brushless DC motor, a high-speed permanent magnet brushless DC motor has the advantages of low noise, high operating efficiency, and a long service life. The research on high-speed permanent magnet brushless DC motors is also consistent with China's development direction toward high efficiency and energy conservation, and thus, these motors have great advantages [2–7].

The research on permanent magnet brushless DC motors is very popular and involves various fields. In the field of deep space satellites, Xu changed the permanent magnet structure of the permanent magnet brushless DC motor into a double coil form and then studied and designed a permanent magnet brushless DC motor using the momentum wheels of micro-nano satellites, which solved the issues of low torque and high power consumption [8]. Peng designed a slot-free, high-speed scheme based on a permanent magnet brushless DC motor and obtained a new type of motor. In addition, for this new type of motor, the influences of different stator slot and rotor pole number combinations on the motor performance were analyzed [9]. Su studied different stator slot and rotor pole combinations, obtained appropriate pole slot combinations through simulation analysis, and designed a permanent magnet brushless DC

motor for the unmanned aerial vehicle (UAV) field [10]. Li studied a brushless DC motor for electric vehicles and optimized the cogging torque of the motor [11]. Kim et al. compared combinations of the stator slot and rotor pole of permanent magnet brushless DC motors and found that the motor with six slots had the best efficiency. In addition, they also compared the magnetization directions of the motor and found that the concentrated magnetization direction had the best efficiency [12]. Bhuvaneswari et al. selected a permanent magnet brushless DC motor with an axial magnetic flux type and designed a permanent magnet brushless DC motor applied to a ceiling fan to conserve power [13]. To reduce the cogging torque in the permanent magnet brushless DC motor, Anuja and Doss adopted asymmetric permanent magnets, which reduced the magnet locking between the stator and rotor [14]. Anuja and Ravikumar et al. also used the finite element analysis method and adjusted the rotor magnetic displacement to reduce the cogging torque in a permanent magnet brushless DC motor [15, 16]. Zuki et al. studied various parameters of different types of permanent magnet brushless DC motors with double-stator structures and concluded that the back electromotive force (EMF) of the permanent magnet brushless DC motor with a double-stator slot rotor structure was the highest [17].

At present, permanent magnet brushless DC motors have high research value and development potential. However, the research on permanent magnet brushless DC motors in the literature described above is not complete, and the stator slot design is lacking. The stator slot structure will have a certain impact on the motor performance. In the design of motor, the most difficult thing to determine is the number of slot pole fit. If not selected properly, it will cause the back potential harmonics to be larger, the cogging moment to be larger, and affect the usability [18, 19]. Therefore, the low-power permanent magnet brushless DC motor was selected as the research object in this study. The stator slot structure of the motor was designed, including the slot-pole combinations and the stator slot type. To study the stator slot type, four different schemes were designed: a pear-shaped ladder slot, pear-shaped round slot, flat-bottom ladder slot, and flat-bottom round slot, and their effects on the cogging torque, reluctance torque, and back EMF were analyzed. The influences of different slot-pole combinations and the stator slot type on the cogging torque, reluctance torque, and back EMF of the permanent magnet brushless DC motor were analyzed using the finite element analysis method and the ANSYS software using a load current excitation source and the motion option setting. Furthermore, the optimal pole/slot ratio and stator slot type were determined.

The results showed that the cogging torque of the 2-stage 24-slot motor was 14 mN•m, and the reluctance torque was 75 mN•m. Moreover, the cogging torque and the reluctance torque of the 2-stage 24-slot motor were the smallest. In addition, the back EMF waveform was the best, resembling a trapezoidal wave; the permanent magnet brushless DC motor stator slot type; the motor cogging torque of the pear-shaped circular slot was the smallest, with a value of 460 mN·m, and the motor reluctance torque of the pear-shaped ladder slot was the smallest, with a value of 1.2 N·m. The conclusion of this study can provide theoretical support for the design of low-power brushless DC motors, especially for the design of small UAV motors.

2. Theory of Operation

2.1. Motor Configuration and Parameters. Guo et al. studied the stator slot and rotor magnetic pole combination of a surface permanent magnet (SPM) motor and analyzed the back EMF and cogging torque of the motor under different slot-pole combinations with 6, 12, 15, 18, 21, 24, 27, 30, and 33 slots and 4, 8, and 10 poles [20]. Therefore, according to the above literature analysis, 4-pole 12-slot, 4-pole 18-slot, 4-pole 24-slot, 4-pole 30-slot, 2-pole 24-slot, 4-pole 24-slot, 6-pole 24-slot, and 8-pole 24-slot slot electrode combinations were selected for this study. Table 1 shows the main structural parameters of a permanent magnet brushless DC motor [21]. The topology of the 4-pole 12-slot motor is shown in Figure 1.

2.2. Analysis. A motor finite element method model was established using the ANSYS software. The pole/slot ratio and stator slot type of the permanent magnet brushless DC motor were analyzed, and the finite element simulation results were obtained. Based on the simulation results, the effects of different slot-pole combinations on the cogging torque, reluctance torque, and back EMF of the motor under the two schemes were analyzed, and the optimal pole/slot ratio and stator slot type were determined. All comparative analyses were performed under a single influence. Accordingly, the Maxwell equation used for FEM analysis is expressed as

$$\frac{\partial}{\partial_x}\left(\nu\frac{\partial A}{\partial_x}\right)+\frac{\partial}{\partial_y}\left(\nu\frac{\partial A}{\partial_y}\right)=-J_Z-\nu\frac{\partial M_y}{\partial_x}+\nu\frac{\partial M_x}{\partial_y}, \quad (1)$$

where A is component of magnetic vector potential, J_Z is the input current density, M_x and M_y are the x- and y-component of magnetization of permanent magnets, and ν is reluctivity.

The cogging torque is an important factor that affects the performance of a permanent magnet brushless DC motor. If the cogging torque is too large, vibrations and noise will be generated during the operation of the motor, which will make the motor unable to operate normally and smoothly and will further affect the overall performance of the motor. The reluctance torque is caused by the magnetic flux deviating from the correct path due to the inconsistency of the direct axis D and the quadrature axis Q. In the same case, the greater the reluctance torque difference between the d-axis and the q-axis is, the greater the corresponding reluctance torque becomes. The reluctance torque can reduce the stator current and improve the out-of-step torque. The overall performance of the motor can be effectively improved by selecting an appropriate value for the reluctance torque. The magnitude of the back EMF affects the efficiency of energy conversion and can reduce the armature current generated

Table 1: Main technical parameters of permanent magnet brushless direct current (DC) motor.

Technical parameter	Data	Technical parameter	Data
Rotor position	Inner rotor	Winding turn-to-turn connection mode	All pole type
Mechanical friction loss (W)	12	Number of parallel branches of winding	1
Air abrasion loss (W)	0	Turns per slot	60
Initial speed (rpm)	1500	Coil pitch	5
Control mode	DC	Number of parallel coils of one turn	1
Outer diameter of stator core (mm)	125	Rotor outer diameter (mm)	79
Inner diameter of stator core (mm)	80	Rotor inner diameter (mm)	31
Actual axial length of stator core (mm)	70	Axial length of rotor (mm)	70
Lamination coefficient of stator core	0.95	Rotor core punching material	M19_24G
Stator core punching material	M19_24G	Lamination coefficient of rotor core	0.95
Number of stator inclined slots	0	Permanent magnet material	XG196/96
Number of winding layers	2	Stator winding material	Copper

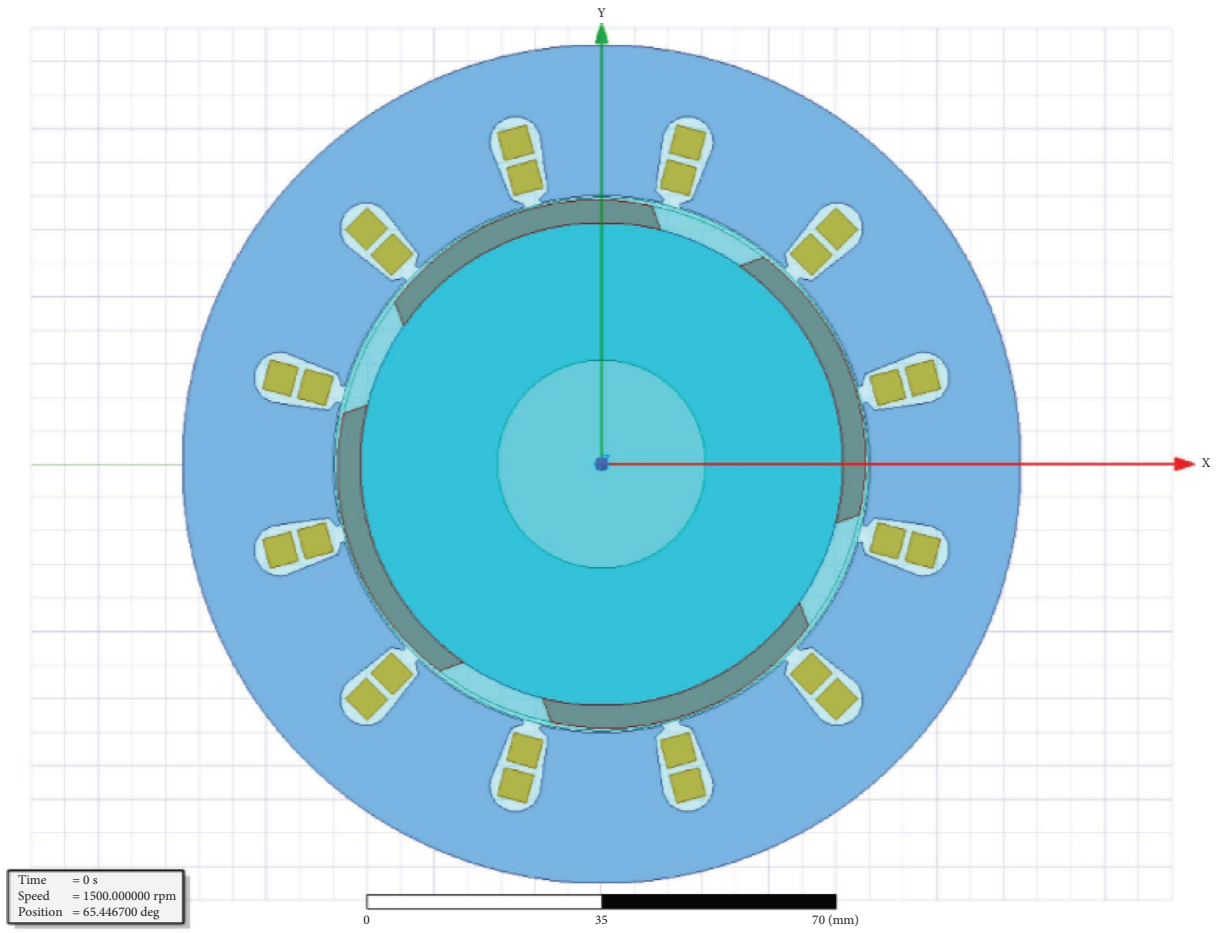

Figure 1: Topology of 4-pole 12-slot motor.

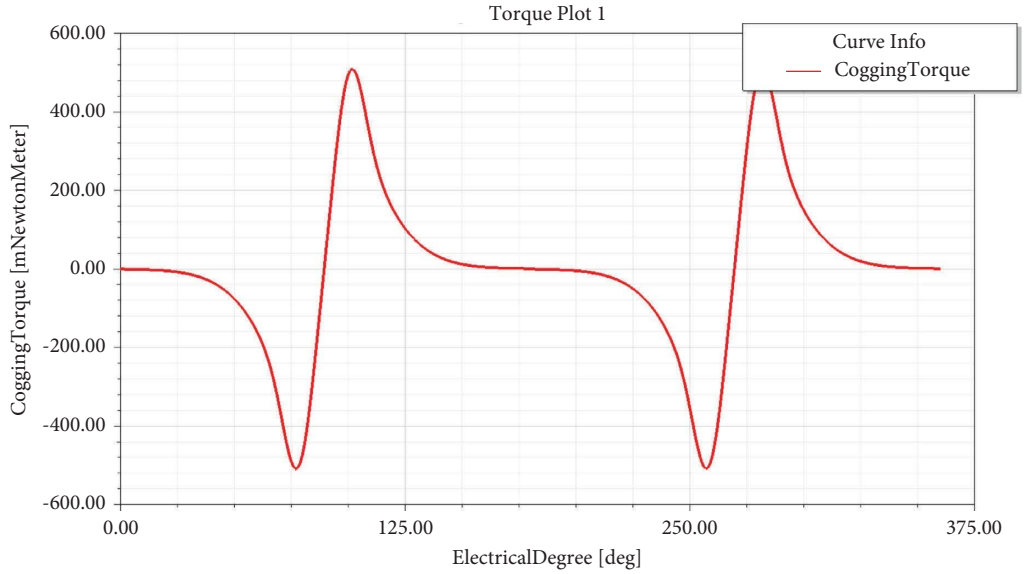

Figure 2: Torque curve of 4-pole 12-slot motor.

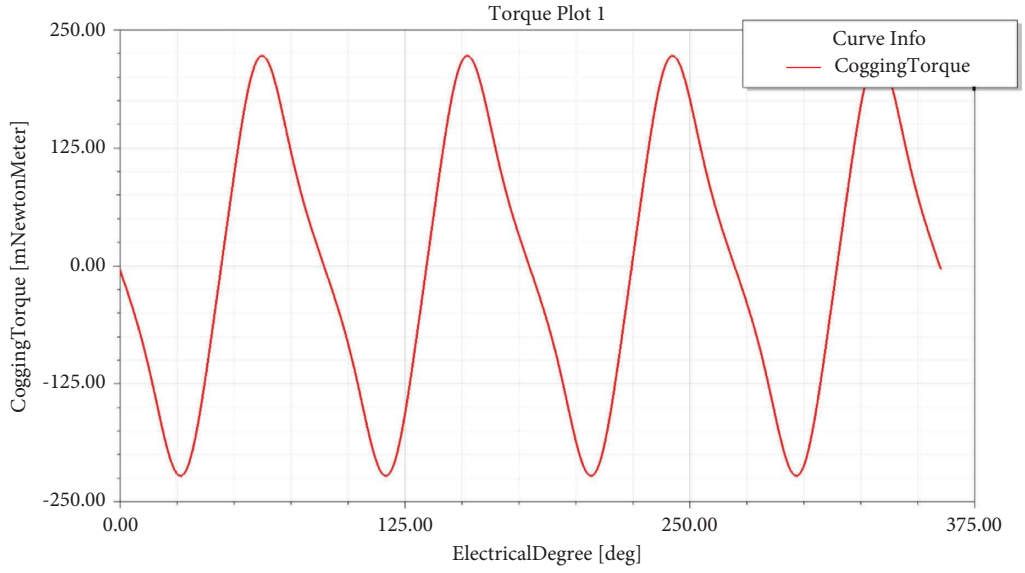

Figure 3: Torque curve of 4-pole 18-slot motor.

during the operation of the motor. If there is no back EMF, it is easy to burn out the motor. A reasonable back EMF value can improve the overall performance of the motor [22]. In the permanent magnet brushless DC motor, the ideal back EMF waveform is a trapezoidal wave.

3. Results and Analysis

3.1. Research on Different Pole Slot Numbers

3.1.1. Cogging Torque. Through the establishment of different slot pole number motor models, under the same working conditions of the motor simulation analysis, the results show that Figures 2–5 show the cogging torque curves for the 4-pole 12-slot, 4-pole 18-slot, 4-pole 24-slot, and 4-pole 30-slot motors, respectively, with maximum cogging torques of 510, 220, 500, and 136 mN·m.

Through comparison and analysis, the 4-pole 30-slot motor had the smallest cogging torque and the best performance, while the 4-pole 12-slot motor had the largest cogging torque and the worst performance. The curves of the motors with different pole slot numbers showed periodic changes. Based on the comparison, the cogging torque curves of the 4-pole 18-slot and 4-pole 30-slot motors were similar to sinusoidal waveforms, and the variation frequencies were also similar and larger.

Figure 6 shows the 2-pole 24-slot cogging torque curve, with a maximum cogging torque of 14 mN·m. Figure 7 shows the 6-pole 24-slot cogging torque curve, with a maximum cogging torque of 780 mN·m. Figure 8 shows the

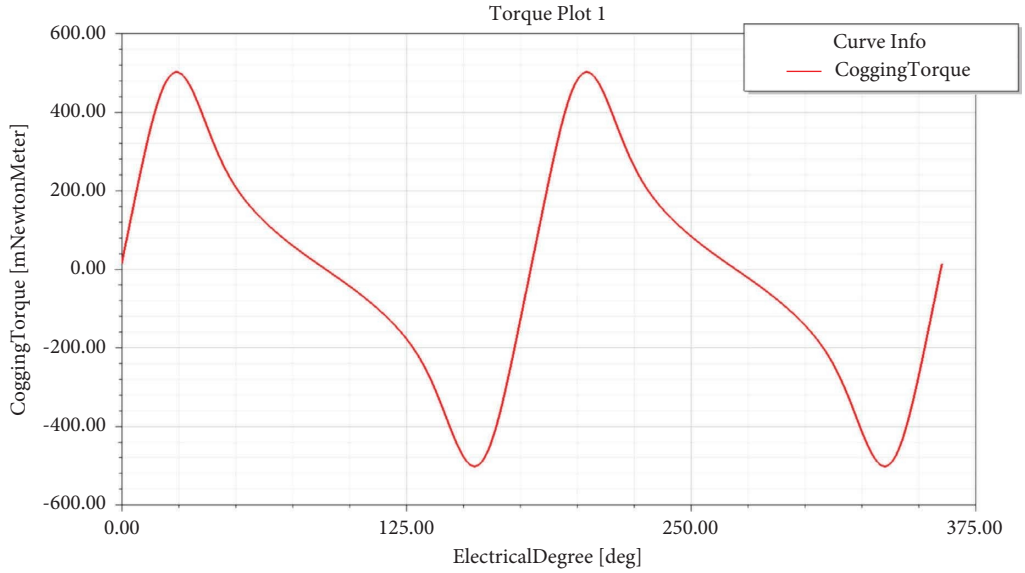

Figure 4: Torque curve of 4-pole 24-slot motor.

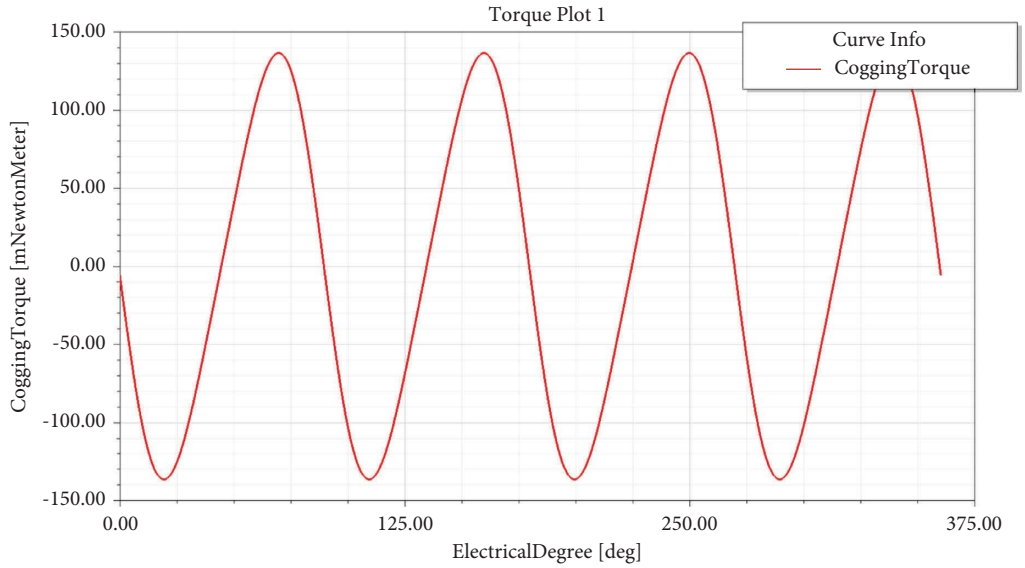

Figure 5: Torque curve of 4-pole 30-slot motor.

8-pole 24-slot cogging torque curve, with a maximum cogging torque of 1.54 mN·m. The 2-pole 24-slot motor exhibited the smallest cogging torque and the best performance, while the 8-pole 24-slot motor exhibited the largest cogging torque and the worst performance. The cogging torque curves of the motors with different pole slots showed periodic changes, and the frequency variations were almost the same. Based on the comparison, the cogging torque curves of the 2-pole 24-slot and 4-pole 24-slot motors were generally similar, and the cogging torque curves of the 6-pole 24-slot and 8-pole 24-slot motors were approximately symmetric in the vertical direction.

3.1.2. Reluctance Torque. Figure 9 shows a graph of the reluctance torque of the 4-pole 12-slot motor, with a maximum value of 1.38 N·m. Figure 10 shows a graph of the reluctance torque of the 4-pole 18-slot motor, with a maximum value of 730 mN·m. Figure 11 shows a graph of the reluctance torque of the 4-pole 24-slot motor, with a maximum value of 1.2 N·m. Figure 12 shows a graph of the reluctance torque of the 4-pole 30-slot motor, with a maximum value of 0.95 N·m. The motor reluctance torque of the 4-pole 12-slot motor was the largest, and the motor reluctance torque of 4-pole 18-slot motor was the smallest. The motor reluctance torque curve of the 4-pole 12-slot

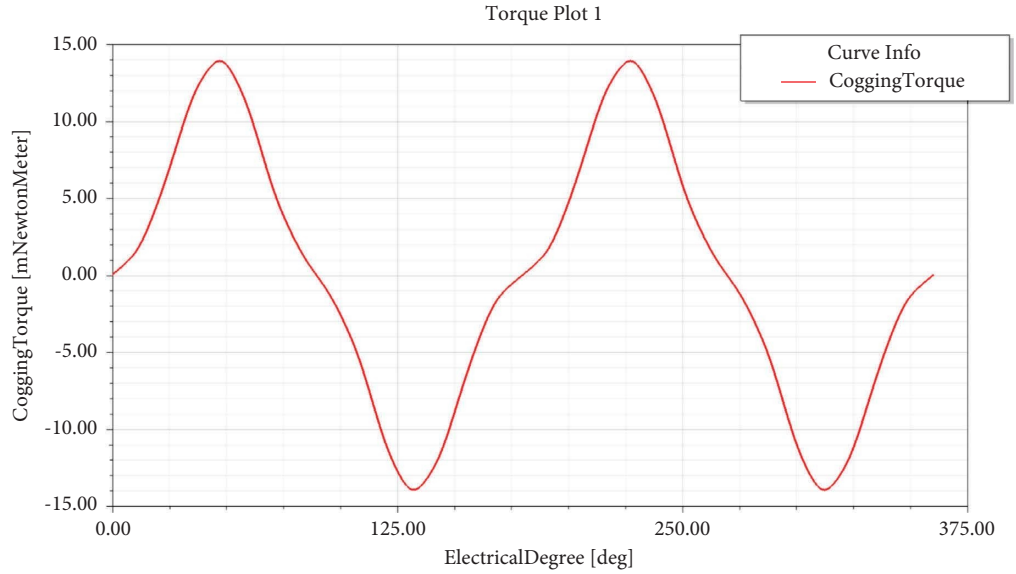

Figure 6: Torque curve of 2-pole 24-slot motor.

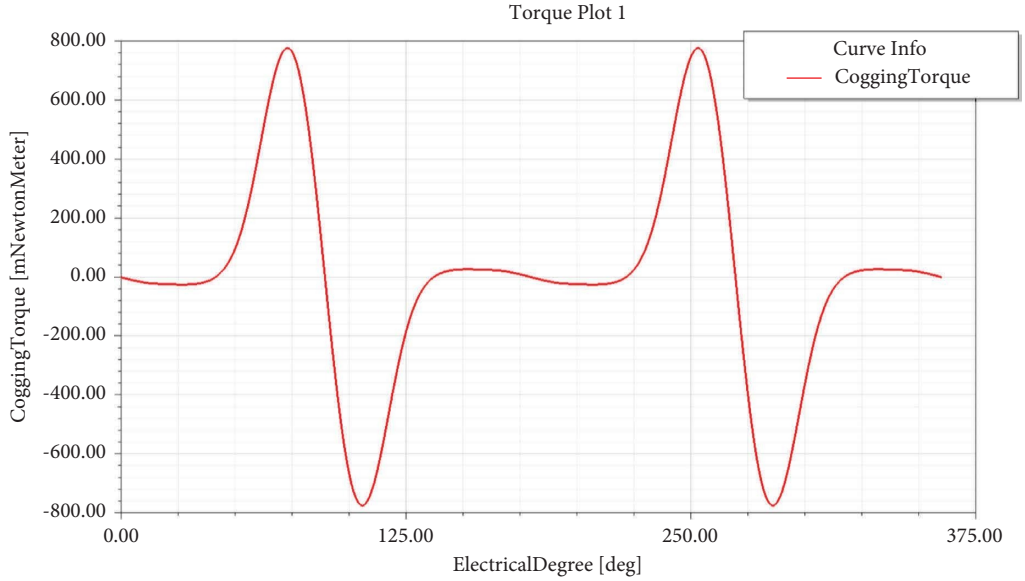

Figure 7: Torque curve of 6-pole 24-slot motor.

motor fluctuated the least, and the motor reluctance torque curve of the 4-pole 30-slot motor fluctuated the most.

Figure 13 shows a graph of the reluctance torque of the 2-poles 24-slot motor, with a maximum value of 75 mN·m. Figure 14 shows a graph of the reluctance torque of the 6-pole 24-slot motor, with the maximum value of 8.5 N·m. Figure 15 shows a graph of the reluctance torque of the 8-pole 24-slot motor, with a maximum value of 3.83 N·m. In addition, the maximum value of the motor reluctance torque of the 4-pole 24-slot motor shown in Figure 12 was 1.2 N·m. The motor reluctance torque of the 6-pole 24-slot motor was the largest, and the motor reluctance torque of the 2-pole 24-slot motor was the smallest.

3.1.3. Back Electromotive Force (EMF). Figure 16 shows a graph of the back EMF of the 4-pole 12-slot motor, with a peak value of 225 V. Figure 17 shows a graph of the back EMF of the 4-pole 18-slot motor, with a peak value of 660 V. Figure 18 shows a 4-pole 24-slot back EMF curve with a peak value of 0.88 kV. Figure 19 shows the back EMF curve of the reluctance torque moment of the 4-pole 30-slot motor, with a peak value of 0.86 kV. Through comparison and analysis, the peak value of the back EMF of the 4-pole 24-slot motor was the largest, and the peak value of the 4-pole 12-slot motor was the smallest. The back EMF curve in Figure 16 is significantly distorted, while those in Figures 17–19 have less distortion. The curves were similar

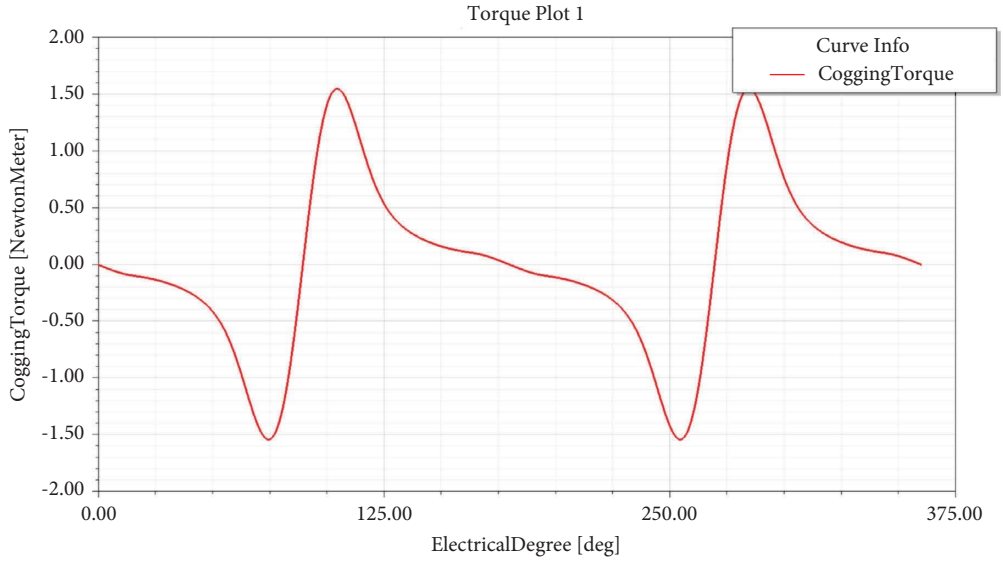

Figure 8: Torque curve 8-pole 24-slot motor.

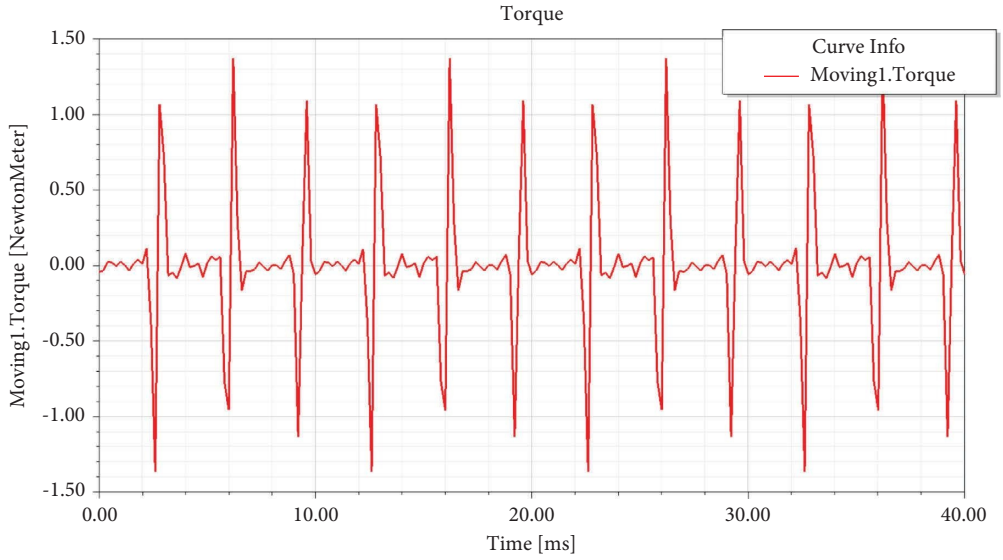

Figure 9: Reluctance torque curve of 4-pole 12-slot motor.

to sine waves, but there were certain deviations from the ideal waveform.

Figure 20 shows the back EMF curve of the 2-pole 24-slot motor, with a peak value of 140 V. Figure 21 shows the back EMF curve of the 6-pole 24-slot motor, with a peak value of 1.36 kV. Figure 22 shows the back EMF curve of the 8-pole 24-slot motor, with a peak value of 0.93 kV. Figure 18 shows that the peak value of the back EMF curve of the 4-pole 24-slot motor was 0.88 kV. The peak value of the back EMF of the 6-pole 24-slot motor was the largest, and the peak value of the 2-pole 24-slot motor was the smallest. The back EMF curve waveform in Figure 20 was similar to a trapezoidal wave, and the waveform was good. The back EMF curve waveform in Figure 22 was significantly distorted. The back EMF curve waveforms in Figures 18 and 21 had no distortion. The curves were similar to sine waves, but there were certain deviations from the ideal waveform.

3.2. Research on Stator Slot. This article studies four types of grooves (Figure 23), namely, pear-shaped ladder groove, pear-shaped circular groove, flat-bottom ladder groove, and flat-bottom circular groove, respectively, and analyses their effects on cutting torque, magnetic resistance moment, and back electromotive force, as well as their effects on motor performance.

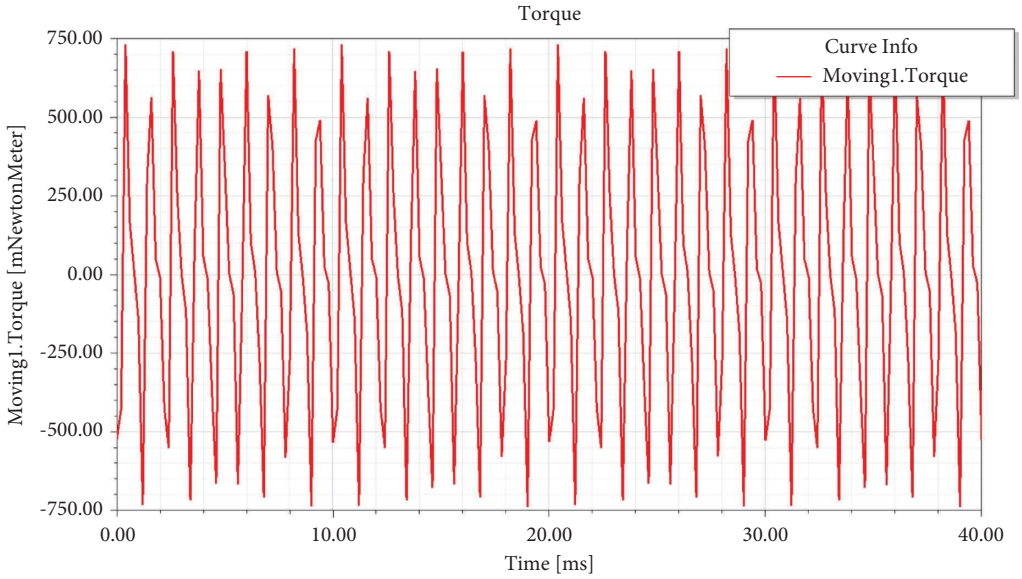

Figure 10: Reluctance torque curve of 4-pole 18-slot motor.

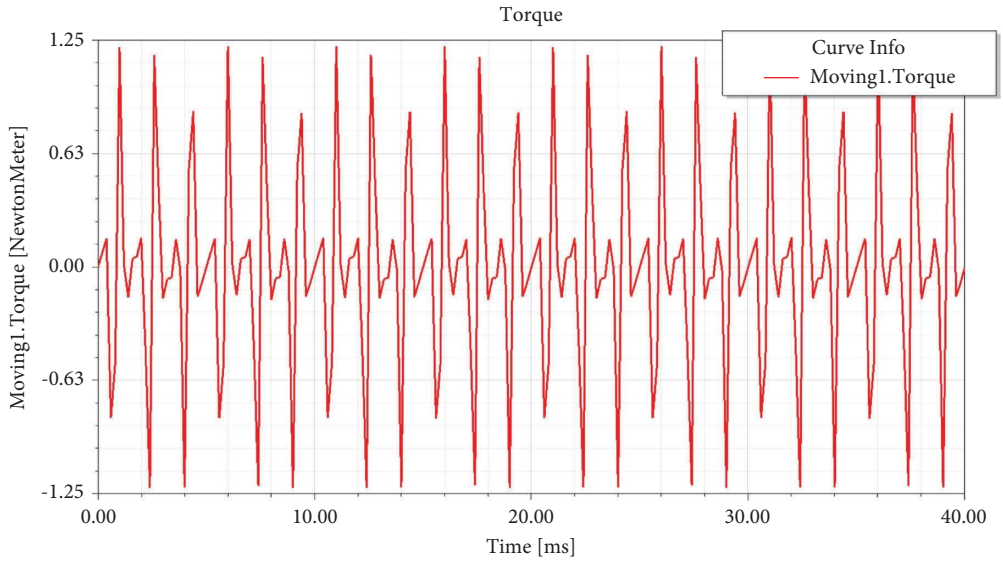

Figure 11: Reluctance torque curve of 4-pole 24-slot motor.

The structure of the pear-shaped ladder slot is shown in Figure 23(a), where Hs0 is 0.6 mm, Hs1 is 1.1 mm, Hs2 is 8.3 mm, Bs0 is 2.6 mm, Bs1 is 5.7 mm, and Bs2 is 7.7 mm. The structure diagram of the pear-shaped round slot is shown in Figure 23(b), where Hs0 is 0.6 mm, Hs2 is 8.3 mm, Bs0 is 2.6 mm, Bs1 is 5.7 mm, and Bs2 is 7.7 mm. The structure diagram of the flat-bottom ladder slot is shown in Figure 23(c), where Hs0 is 0.6 mm, Hs1 is 1.1 mm, Hs2 is 8.3 mm, Bs0 is 2.6 mm, Bs1 is 5.7 mm, Bs2 is 7.7 mm, and Rs is 0 mm. The structure diagram of the flat-bottom round slot is shown in Figure 23(d), where Hs0 is 0.6 mm, Hs1 is 1.1 mm, Hs2 is 8.3 mm, Bs0 is 2.6 mm, Bs1 is 5.7 mm, Bs2 is 7.7 mm, and Rs is 0 mm.

3.2.1. Cogging Torque. Figure 24 shows the torque curve of the pear-shaped slot motor, with a maximum value of 500 mN·m. Figure 25 shows the cogging torque curve of the pear-shaped circular slot motor, with a maximum value of 460 mN·m. Figure 26 shows the cogging torque curve of the flat-bottom ladder slot motor, with a maximum value of 520 mN·m. Figure 27 shows the cogging torque curve of the flat-bottom circular slot motor, with a maximum value of 520 mN·m. The cogging torque of the motor with the pear-shaped circular slot was the smallest, and the motor performance was the best, while the cogging torque of the motor with the flat-bottom ladder and circular slot was the largest, and the motor performance was the worst. The curves of the

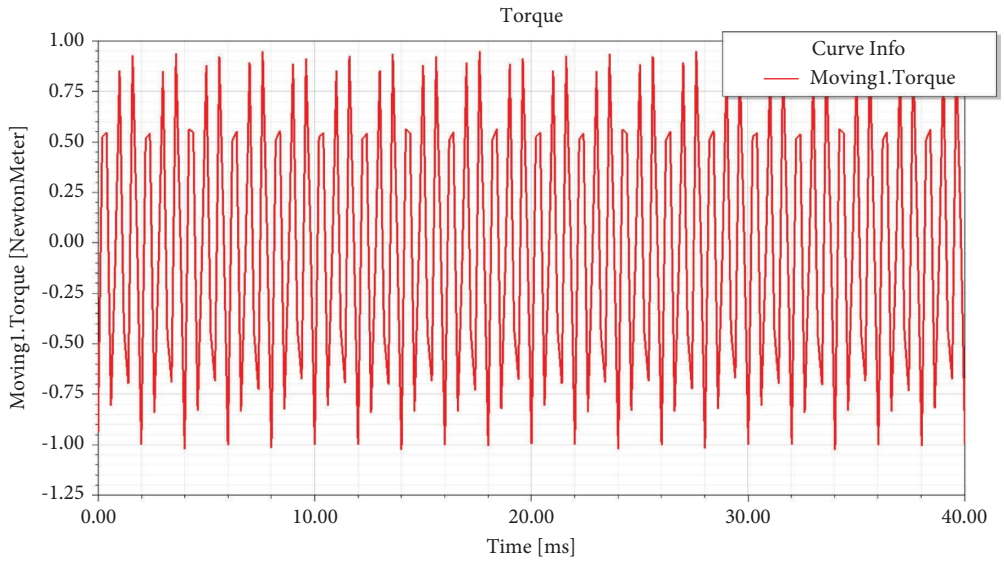

Figure 12: Reluctance torque curve of 4-pole 30-slot motor.

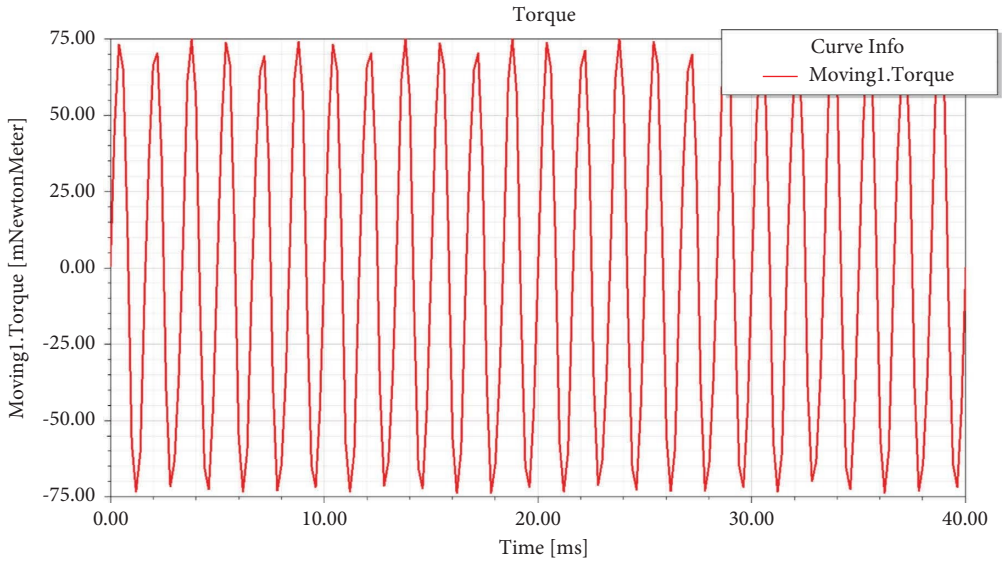

Figure 13: Magnetic resistance torque curve of 2-pole 24-slot motor.

other four motors with different stator slot types were similar and showed periodic variations.

3.2.2. Reluctance Torque. Figure 28 shows a graph of the reluctance torque of the pear-shaped ladder slot motor, with a maximum value of 1.2 N·m. Figure 29 shows a graph of the reluctance torque of the pear-shaped circular slot motor, with a maximum value of 1.35 N·m. Figure 30 shows a graph of the reluctance torque of the flat-bottom ladder slot motor, with a maximum value of 1.27 N·m. Figure 31 shows a graph of the reluctance torque of the flat-bottom circular slot motor, with a maximum value of 1.28 N·m. Through comparison and analysis, the motor reluctance torque of the flat-bottom round-mouth groove was the largest, and the motor reluctance torque of the pear-shaped ladder-mouth

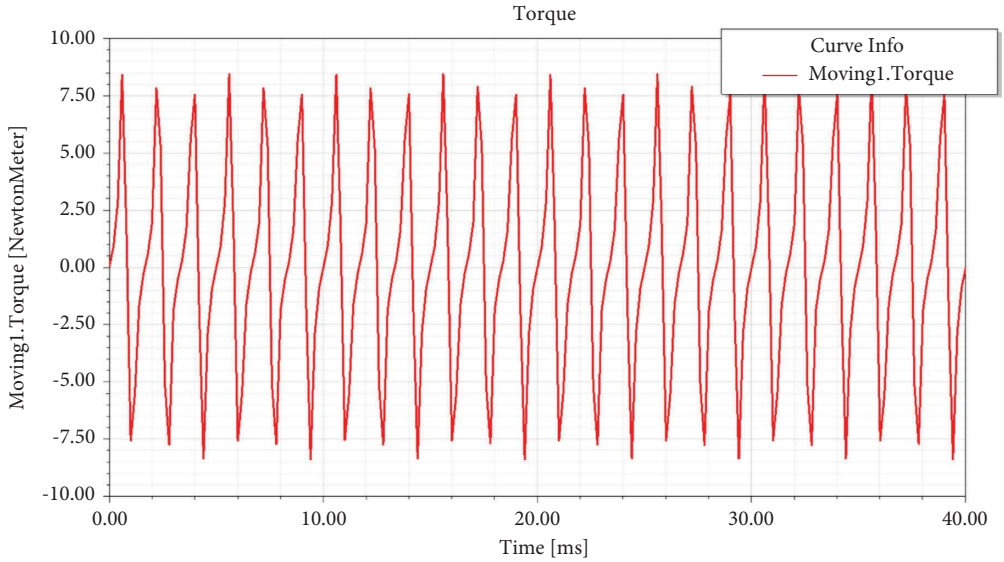

Figure 14: Magnetic resistance torque curve of 6-pole 24-slot motor.

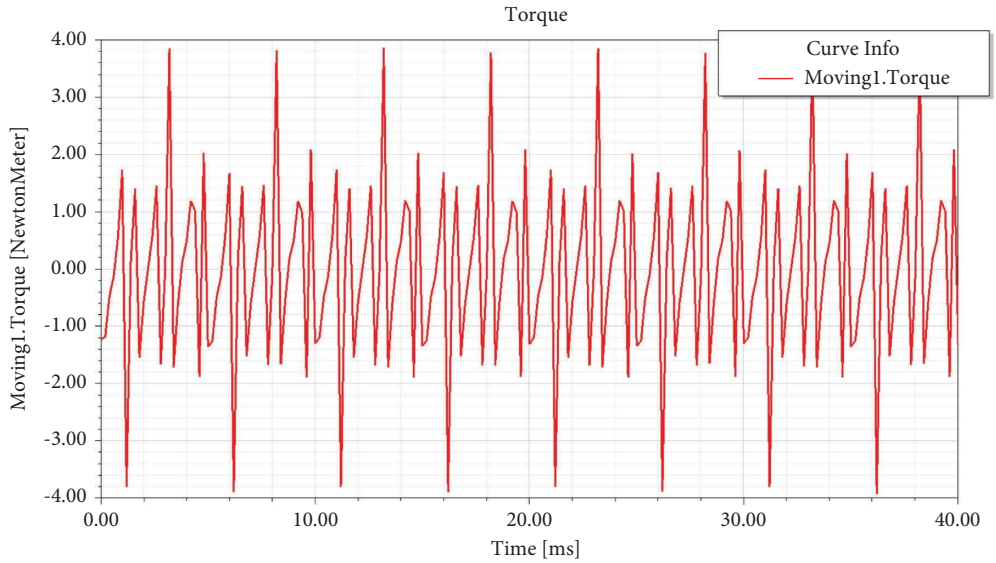

Figure 15: Magnetic resistance torque curve of 8-pole 24-slot motor.

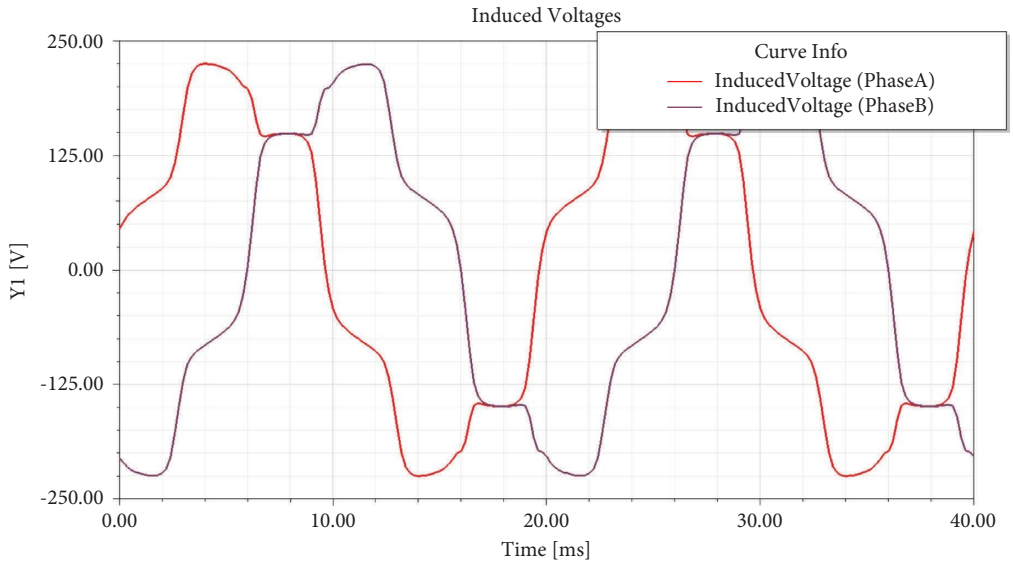

Figure 16: Back electromotive force (EMF) curves of 4-pole 12-slot motor.

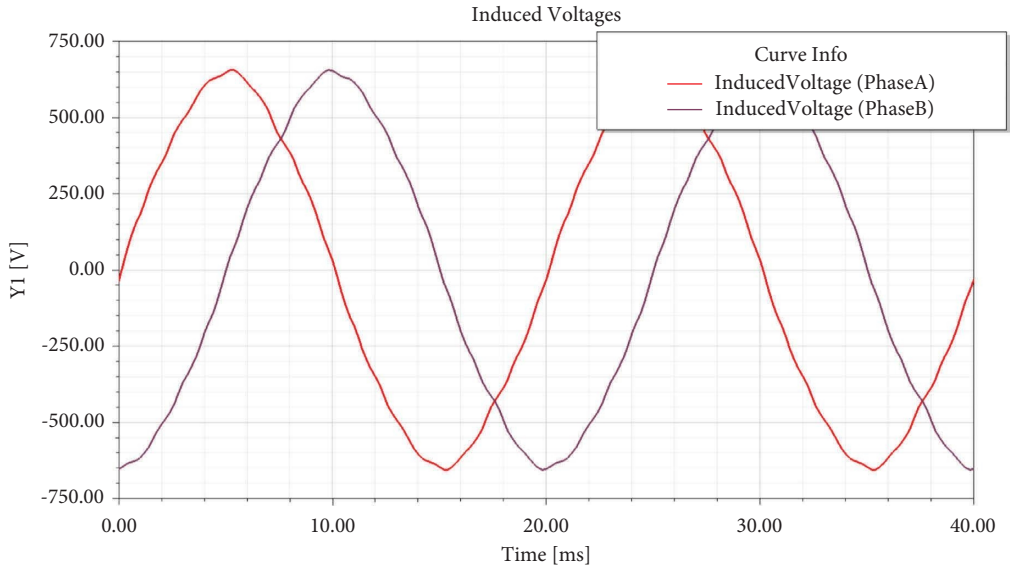

Figure 17: Back EMF curves of 4-pole 18-slot motor.

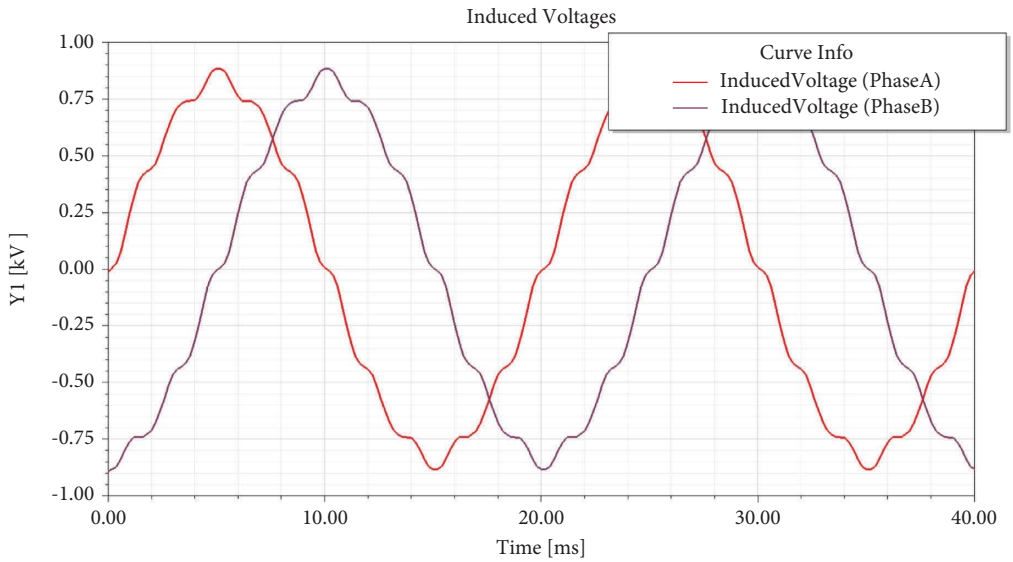

Figure 18: Back EMF curves of 4-pole 24-slot motor.

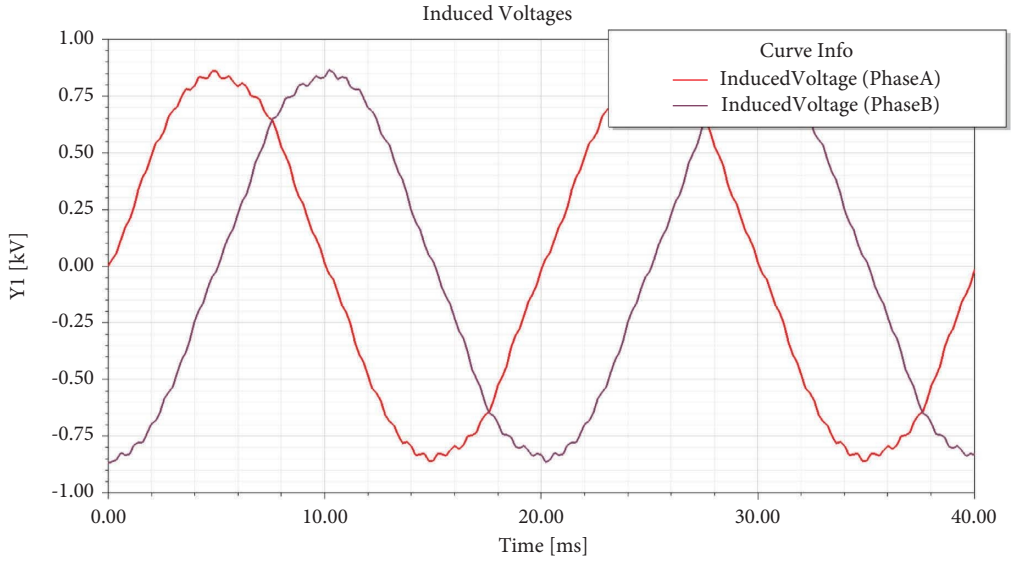

Figure 19: Back EMF curves of 4-pole 30-slot motor.

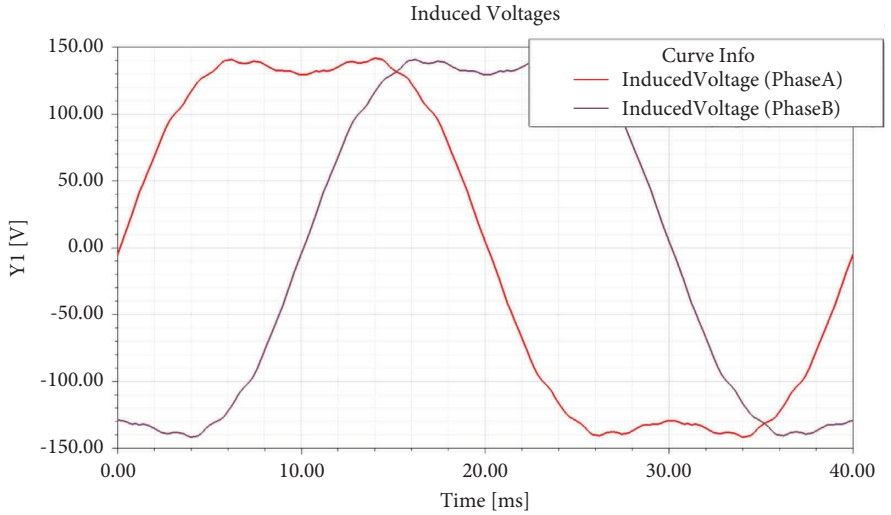

Figure 20: Back EMF curve of 2-pole 24-slot motor.

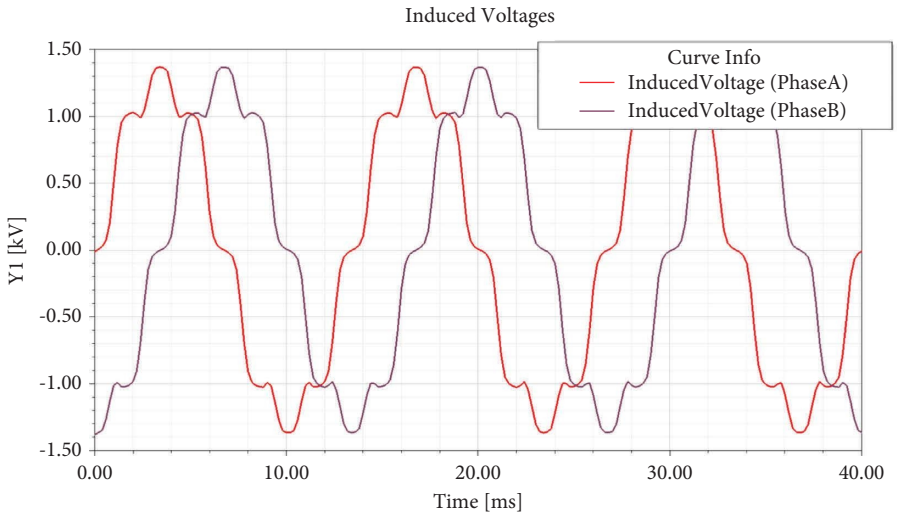

Figure 21: Back EMF curve of 6-pole 24-slot motor.

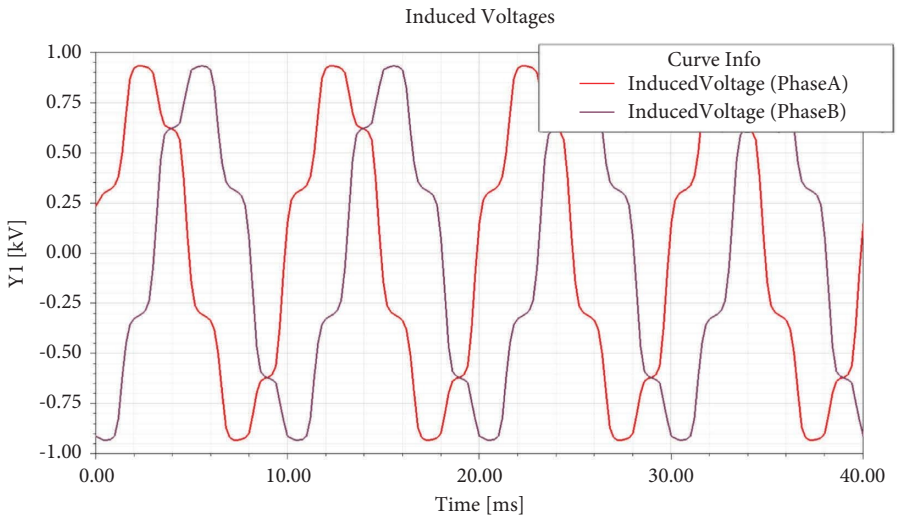

Figure 22: Back EMF curve of 8-pole 24-slot motor.

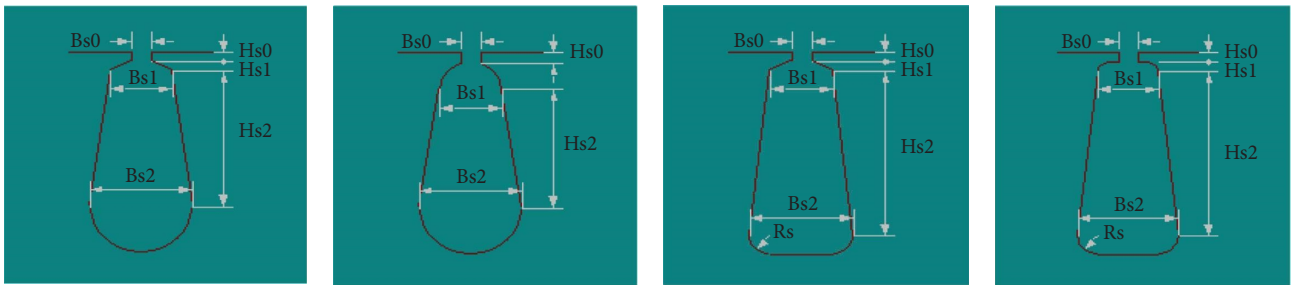

Figure 23: Four different types of slot patterns. (a) Pear-shaped ladder slot. (b) Pear-shaped round slot. (c) Flat-bottom ladder slot. (d) Flat-bottom round slot.

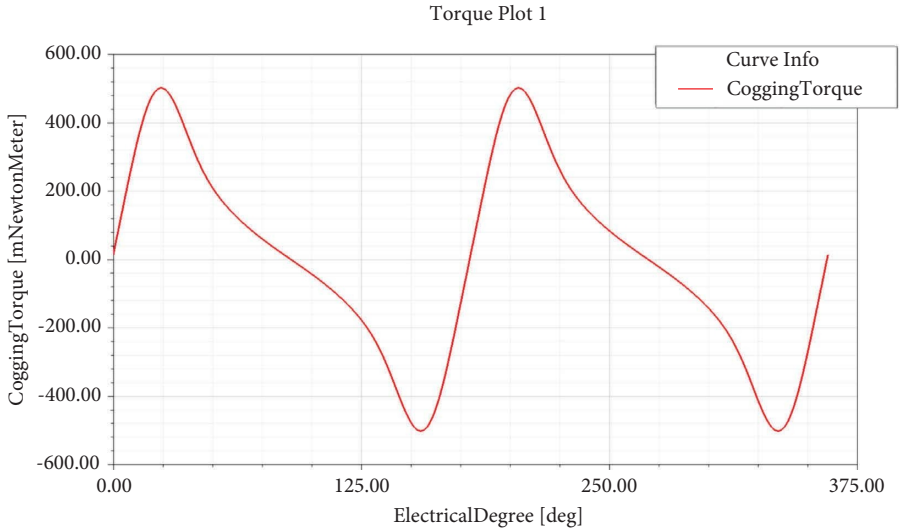

Figure 24: Cogging torque of pear-shaped slot motor.

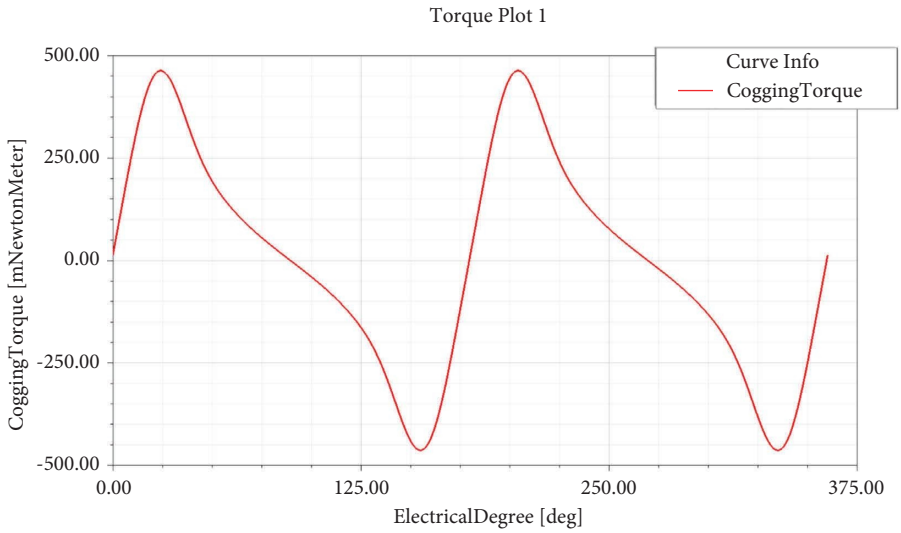

Figure 25: Cogging torque of pear-shaped circular slot motor.

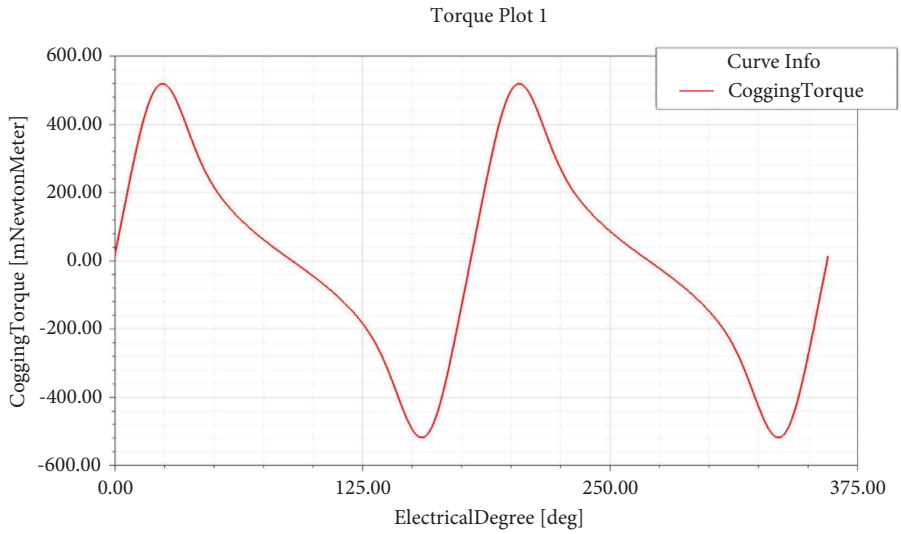

Figure 26: Cogging torque of flat-bottom ladder slot motor.

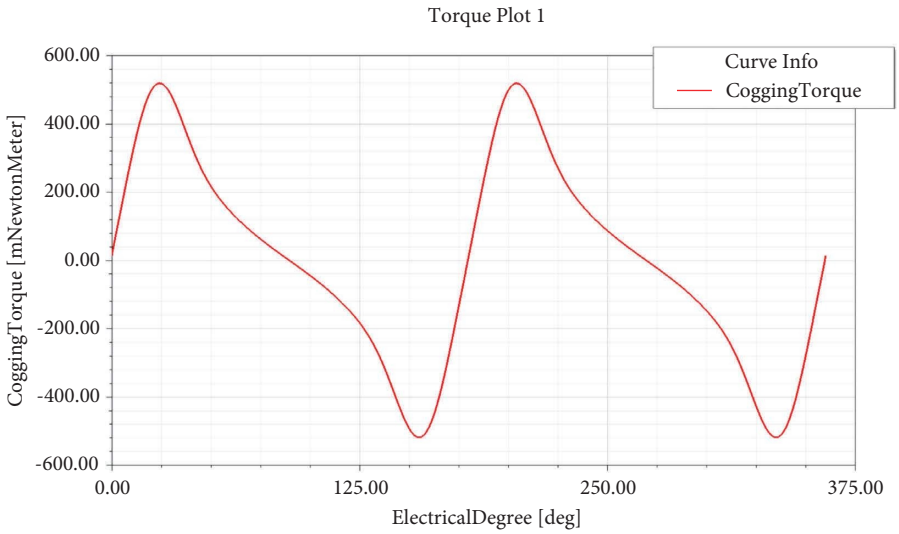

Figure 27: Cogging torque of flat-bottom circular slot motor.

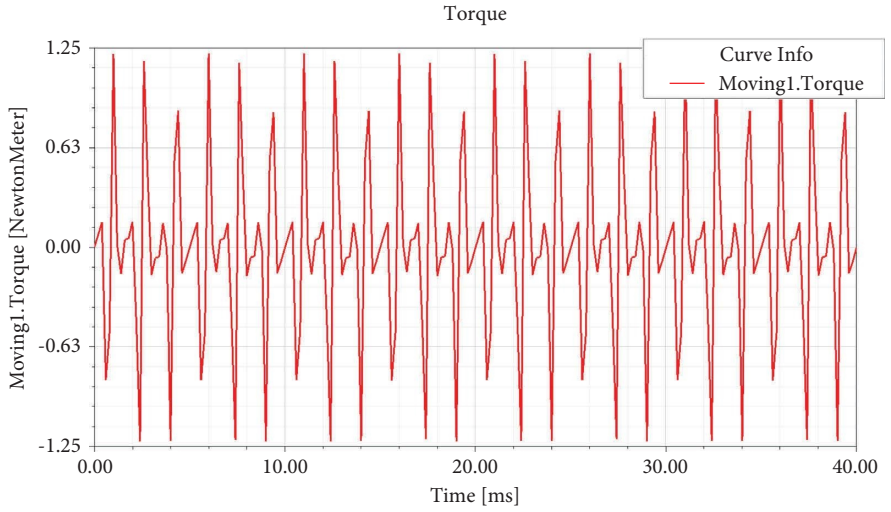

Figure 28: Magnetic resistance torque curve of pear-shaped ladder slot motor.

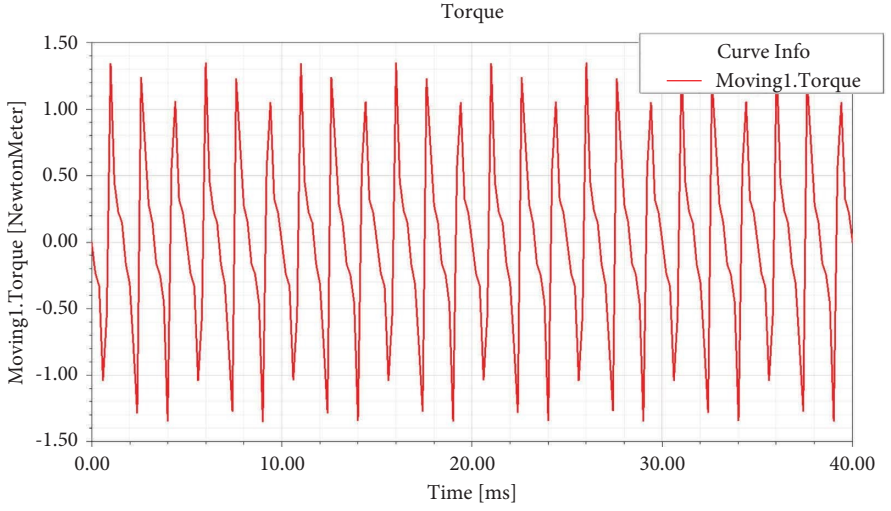

Figure 29: Magnetic resistance torque curve of pear-shaped circular slot motor.

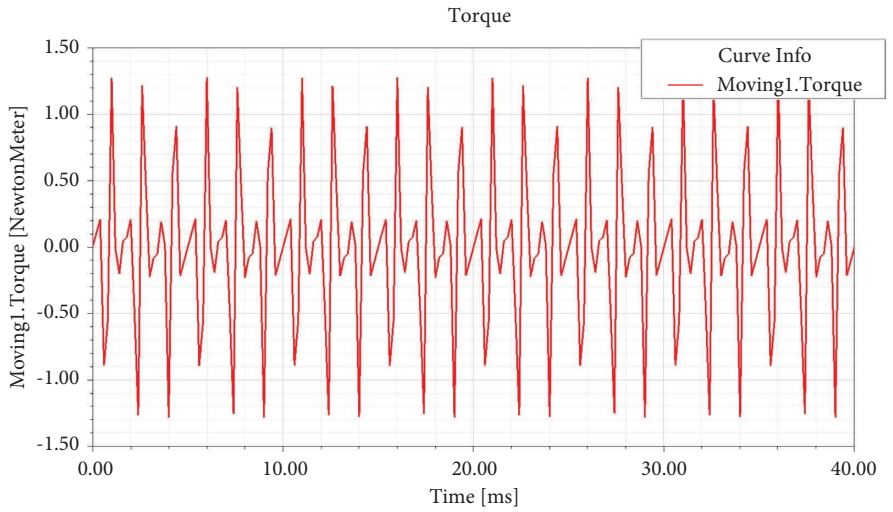

Figure 30: Magnetic resistance torque curve of flat-bottom ladder slot motor.

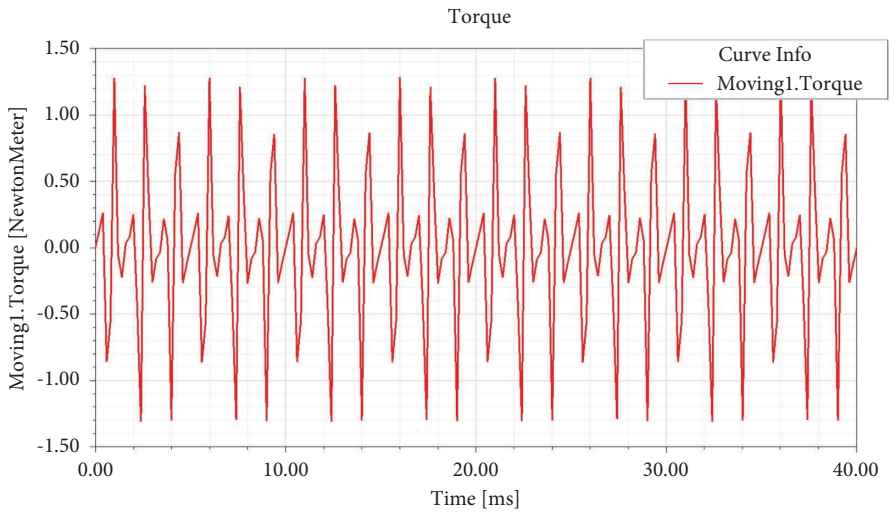

Figure 31: Magnetic resistance torque curve of flat-bottom circular slot motor.

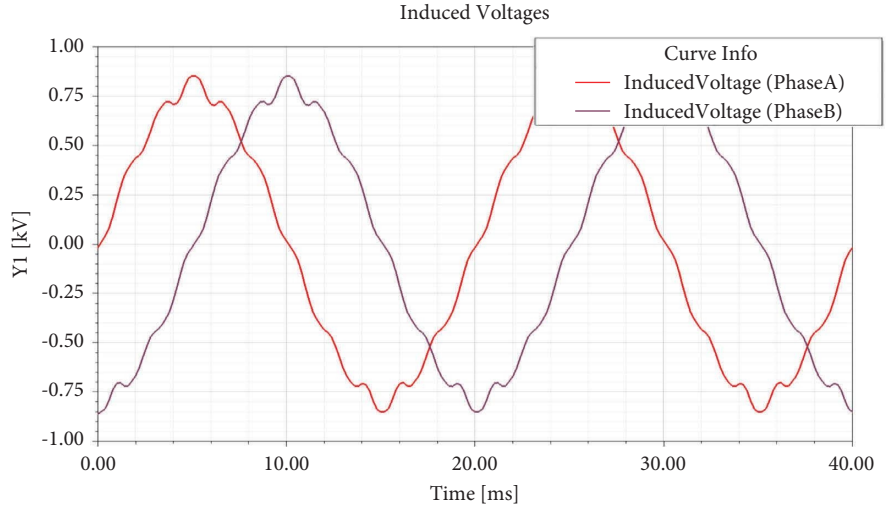

Figure 32: Back EMF curve of pear-shaped ladder slot motor.

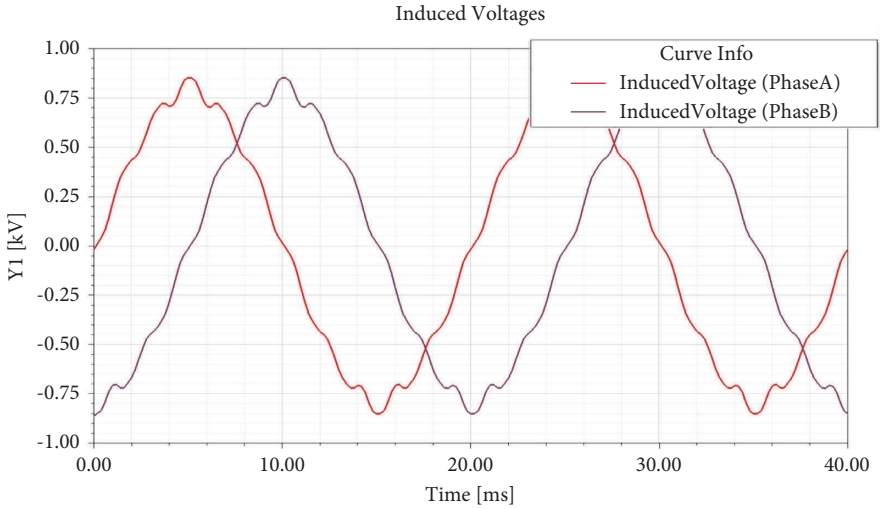

Figure 33: Back EMF curve of pea-shaped circular slot motor.

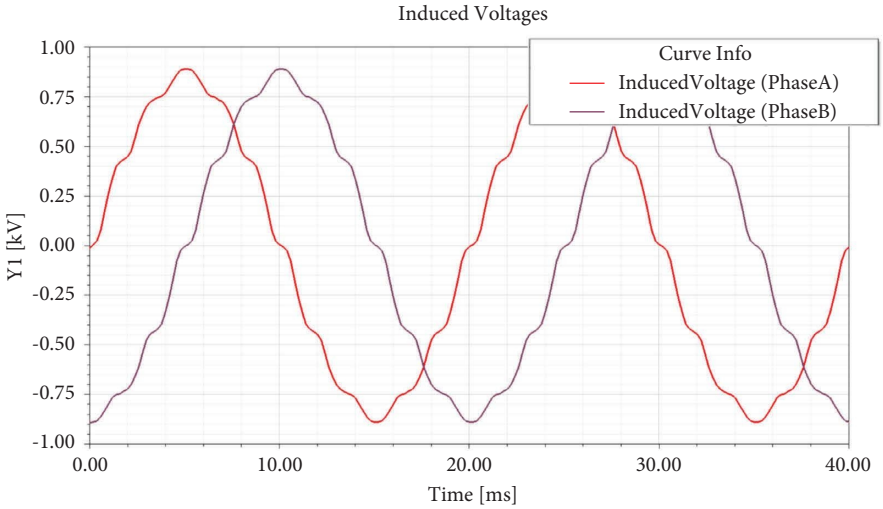

Figure 34: Back EMF curve of flat-bottom ladder slot motor.

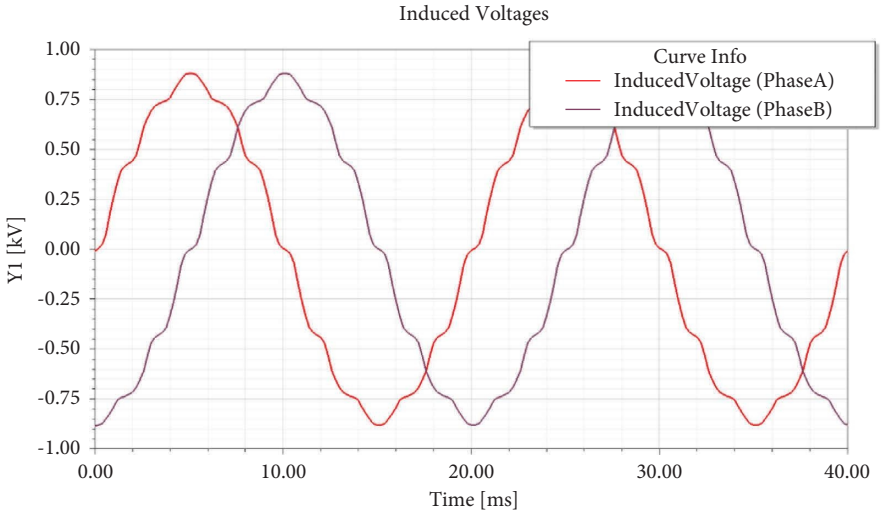

Figure 35: Back EMF curve of flat-bottom circular slot motor.

groove was the smallest. In addition, the motor reluctance torque curves of the pear-shaped ladder-mouth groove, the flat-bottom ladder-mouth groove, and the flat-bottom round-mouth groove were similar.

Figure 32 shows the back EMF curve of the pear-shaped ladder slot motor, with a peak value of 0.88 kV. Figure 33 shows the back EMF curve of the pear-shaped circular slot motor, with a peak value of 0.85 kV. Figure 34 shows the back EMF curve of the flat-bottom ladder slot motor, with a peak value of 0.89 kV. Figure 35 shows the back EMF curve of the flat-bottom circular slot motor, with a peak value of 0.87 kV. The peak values of the back EMFs for these four different stator slot motors were similar. Furthermore, the curve waveforms of the back EMF were similar, and there was little distortion. The curve waveforms were similar to sine waves, but there were certain deviations from the ideal waveform.

4. Conclusions

This article examined the stator slot structure of a permanent magnet brushless DC motor in terms of the slot number and stator slot type, and their effects on the cogging torque, reluctance torque, and back EMF were analyzed. The following conclusions were obtained:

(a) The effect of the pole-slot ratio on the cogging torque, reluctance torque, and back EMF of a low-power brushless DC motor is analyzed by simulation. The results show that the 2-pole and 24-slot schemes have relatively excellent performances.

(b) In the study of the numbers of slots and poles of the permanent magnet brushless DC motor, the cogging torque of the 2-stage, 24-slot motor was 14 mN·m, and the reluctance torque was 75 mN·m. Moreover, the cogging torque and the reluctance torque of the 2-stage, 24-slot motor were the smallest. In addition, the back EMF waveform was the best, resembling a trapezoidal wave.

(c) In the study of the permanent magnet brushless DC motor stator slot type, the motor cogging torque of the pear-shaped circular slot was the smallest, with a value of 460 mN·m, and the motor reluctance torque of the pear-shaped ladder slot was the smallest, with a value of 1.2 N·m. However, the back EMF waveforms of four different stator slot types were similar and adequate.

(d) In the design of low-power brushless DC, 2-pole, and 24-slot can be preferred. Moreover, the slot shape does not appreciably affect the motor performance.

Data Availability

Some or all data, models, or code generated or used during the study are available in a repository or online in accordance with funder data retention policies.

Conflicts of Interest

The authors declare that they have no conflicts of interest.

Authors' Contributions

C.Z. and R.L. wrote the original draft and developed methodology. R.L. and T.P. were in charge of data curation and investigation. C.M. supervised the study and wrote and reviewed the article. G.Z. was in charge of software and visualization. All authors read and agreed to the published version of the manuscript.

Acknowledgments

This work was supported by the Water Conservancy Science and Technology Projects in Zhejiang Province (grant no. RC2220) and the Open Found of Key Laboratory for Technology in Rural Water Management of Zhejiang Province (grant no. ZJWEU-RWM-20200404B). The authors thank the support of "Nanxun Young Scholars." The authors thank LetPub (http://www.letpub.com (accessed on 7 September 2022)) for its linguistic assistance during the preparation of this manuscript.

References

[1] K. Vanchinathan, K. R. Valluvan, C. Gnanavel, and C. Gokul, "Design methodology and experimental verification of intelligent speed controllers for sensorless permanent magnet Brushless DC motor," *Int Trans Electr Energ Syst*, vol. 31, no. 9, Article ID e12991, 2021.

[2] J. Jing and Y. Zhu, "Research progress and trend analysis of Brushless DC motor," *Journal of Jiujiang University (Natural Science Edition)*, vol. 37, no. 01, pp. 7–14, 2022.

[3] X. Liu, "Discussion on optimal design of high speed permanent magnet brushless DC motor," *Internal combustion engine and accessories*, vol. 06, no. 12, pp. 96-97, 2020.

[4] M. Yuan, "Application status and development trend of brushless motor," *Metallurgical management*, vol. 03, no. 05, 2019.

[5] X. Zhou, "Application and development analysis of Brushless DC motor in industry," *Modern industrial economy and informatization*, vol. 11, no. 03, pp. 97-98, 2021.

[6] Y. Ju, Z. Xu, D. Zhang, and Y. Shi, "Research on the number of slot poles and rotor magnetic circuit structure of 12 slot 10 pole permanent magnet motor," *Micro special motor*, vol. 49, no. 05, pp. 11–14, 2021.

[7] S. Li, L. Ju, and Y. Yang, "Structural design of small power permanent magnet brushless DC motor," *Scientific and technological innovation*, vol. 10, no. 30, pp. 138–140, 2018.

[8] K. Xu, *Design of Permanent Magnet Brushless DC Motor for Momentum Wheel of Micro Nano Satellite*, Beijing Institute of petroleum and chemical engineering, Beijing China, 2021.

[9] Y. Peng, *Design and Optimization of Slot Less High Speed Permanent Magnet Brushless DC Motor*, Shenyang University of Technology, Shenyang China, 2021.

[10] X. Su, *Design and Optimization of Permanent Magnet Brushless DC Motor for UAV*, Qufu Normal University, Shandong, China, 2020.

[11] M. Li, *Design and Cogging Torque Optimization of Brushless DC Motor for Electric Vehicles*, Jiangsu University, Zhenjiang China, 2019.

[12] H. S. Kim, J. W. Kwon, and B. I. Kwon, "Investigation of slot-pole combinations on IPM BLDC motor considering magnetization direction," *International Journal of Applied Electromagnetics and Mechanics*, vol. 60, no. 4, pp. 603–872, 2019.
[13] S. Bhuvaneswari, P. Sivaraman, N. Anitha, and A. Matheswaran, "Optimized design of permanent magnet brushless DC motor for ceiling fan applications," *Materials Today Proceedings*, vol. 45, pp. 1081–1086, 2021.
[14] T. A. Anuja and M. A. N. Doss, "Asymmetrical magnets in rotor structure of a permanent magnet brushless DC motor for cogging torque minimization," *Journal of Electrical Engineering & Technology*, vol. 17, no. 2, pp. 1271–1279, 2022.
[15] T. A. Anuja and M. A. N. Doss, "Reduction of cogging torque in surface mounted permanent magnet brushless DC motor by adapting rotor magnetic displacement," *Energies*, vol. 14, no. 10, p. 2861, 2021.
[16] B. V. Ravikumar, K. Sivakumar, and S. Karunanidhi, "Design of a high power density Halbach BLDC motor for an electric vehicle propulsion," *Int Trans Electr Energ Syst*, vol. 31, no. 6, Article ID e12869, 2021.
[17] N. A. M. Zuki, R. N. F. K. R. Othman, S. R. C. Ahmad, and F. A. A. Shukor, "Consideration of various constants in double stator permanent magnet brushless DC motor," *International Journal of Applied Electromagnetics and Mechanics*, vol. 63, no. 1, pp. 1–17, 2020.
[18] J. Tan, "Study on the combination law of slot Pole number of fractional slot concentrated winding of three-phase brushless DC motor (serial II)," *Micro*, vol. 52, no. 01, pp. 52–56, 2008.
[19] X. Su, *Design and Optimization of UAV Permanent Magnet Brushless DC Motor*, Shandong, Qufu Normal University, Jining, China, 2020.
[20] L. Guo and H. Wang, "Research on stator slot and rotor Pole combination and Pole arc coefficient in a surface-mounted permanent magnet machine by the finite element method," *World Electric Vehicle Journal*, vol. 12, no. 1, p. 26, 2021.
[21] A. Zhao, *Research and Design of a Miniwatt Permanent Magnet Brushless DC Motor. Guangxi*, Guilin University of Technology, Guilin, China, 2017.
[22] K. Chakkarapani, T. Thangavelu, and K. Dharmalingam, "Thermal analysis of brushless DC motor using multiobjective optimization," *Int Trans Electr Energ Syst*, vol. 30, no. 10, Article ID e12546, 2020.